nature physics

Supplementary information

https://doi.org/10.1038/s41567-024-02558-1

Sequence-specific interactions determine viscoelasticity and ageing dynamics of protein condensates

In the format provided by the authors and unedited

Table of contents

This PDF file includes:

Supplementary Materials and Methods

Protein construct design and purification

All A1-LCD constructs were based on residues 186-320 of human hnRNPA1 (UniProt: P09651; Isoform A1-A). The coding sequences for the variants were synthesized (by ThermoFisher) with the inclusion of the coding sequence for an N-terminal TEV cleavage site and flanking attB sites. The sequences were then subcloned into a pDEST17 vector using LR clonase (ThermoFisher). Proteins were expressed and purified (Supplementary Fig. S1) as previously described [1] with a few modifications. The purification of tryptophan-containing variants was modified as follows: the Nickel-affinity column buffers contained 6 M Urea instead of 4 M, TEV cleavage was conducted at room temperature with 3 M Urea instead of 2 M, and the GdmHCl concentration in the size exclusion buffer was increased to 4 M. Additionally, the protein concentration of the allW variant had to be kept below 50 μM during TEV cleavage to prevent precipitation. The amino acid sequences of each of the constructs are shown in **Table S1**.

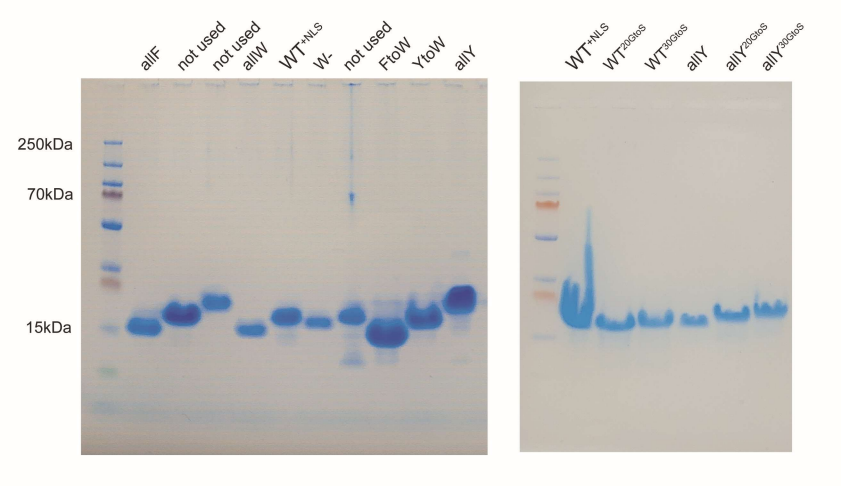

Supplementary Figure S1. SDS-PAGE (sodium dodecyl sulfate–polyacrylamide gel electrophoresis) gel image of purified proteins used for the experiments. Gels were NuPage 4-12% gradient Bis-Tris gel from Invitrogen. The gel was run using NuPage MES-SDS running buffer from Invitrogen at 160V for 50 min. The Ladder is PageRuler Plus Prestained Protein ladder from Thermo Scientific. The gel was washed with water and stained with SimplyBlue SafeStain from Novex using the standard method.

Measurements to construct phase boundaries

Buffer exchange into native buffer without excess salt and measurements of phase boundaries were performed as described previously [2]. Phase separation of A1-LCD solutions was induced by adding NaCl to a final concentration of 150 mM. Dilute phase concentrations as a function of temperature were determined in triplicate as outlined in previous work [2,3]. Briefly, the dilute phase was separated from the dense phase via centrifugation, diluted if the desired temperature was above ambient values, and the concentration was determined via standard UV-VIS absorbance measurements. Dilute phase concentrations at or above 30°C were determined via cloud point measurements using static light scattering as previously described [2,4].

Glass slide and coverslip preparation

Glass slides and coverslips were either coated with Tween20 or with Sigmacote (Sigma-Aldrich). To coat with Tween20, we followed the procedure of Alshareedah et al. [5] Briefly, glass

slides and coverslips were immersed in a 20% vol/vol solution of Tween20 for 30 minutes. Next, the glass slides and coverslips were washed with milliQ water several times and subsequently dried with compressed air. For Sigmacote coating, the slides and coverslips were first cleaned with 70% ethanol and then coated with Sigmacote following the manufacturer's procedure.

Sample preparation and chamber assembly

Samples were prepared by mixing appropriate volumes of 20 mM HEPES buffer pH 7 (adjusted with ammonium hydroxide), buffer exchanged protein, and yellow-green carboxylate-modified polystyrene beads (FluoSpheres, Invitrogen). The bead diameter was 0.2 μm, 1 μm, and 2 μm for video particle tracking, passive microrheology with optical tweezers, and creep test measurements, respectively. 1.5 M NaCl was then added to a final concentration of 150 mM to induce phase separation. 2 to 5 μL of the prepared sample was spotted onto a coverslip and sandwiched with a glass slide using 3 to 4 layers of double-sided tape. Mineral oil was then injected into the chamber to prevent the sample from evaporation by filling the remaining volume and isolating the sample from air.

DIC Microscopy and ThT assay

Differential interference contrast microscopy (DIC) and ThT fluorescent images were obtained at room temperature using a Zeiss 780 LSM confocal microscope with a 20× objective. Samples were prepared as described above. Protein concentrations were selected to ensure they were above the c_{sat} of the corresponding variant at room temperature. 4 μL of the protein solution with 20 μM of ThT was applied to the slide and imaged at the indicated times. The ThT was excited with a 480 nm laser.

Fourier Transform Infrared (FTIR) Spectroscopy

The FTIR data were collected using a Nicolet iS20 FTIR instrument (ThermoFisher Scientific) with a Smart iTX Diamond accessory. For dense phase measurements phase separation was induced in 200 to 500 μL of 1 to 2 mM stock solutions of protein in 20 mM HEPES pH 7 by adding NaCl to a final concentration of 150 mM. The samples were then centrifuged at 5000 RCF for 5 min. A 3 μL sample of dense phase was transferred to the stage using a positive displacement pipette. The dilute phase was then pipetted around the dense phase and the sample was sealed with the liquid chamber accessory to prevent desiccation. The insulin fibrils were centrifuged and washed with deionized water 5 times, and then transferred to the stage for analysis. Each FTIR spectrum represents the average of 64 consecutive scans, with a resolution of 0.2411 cm^{-1}. A blank of 20 mM HEPES pH 7 with 150 mM NaCl using the same scan and resolution settings was subtracted from each spectrum. The spectra were checked for an appropriate ratio of amide I and II band intensity, low noise, and the absence of other artifacts to confirm proper data acquisition and background subtraction. Data were analyzed using OriginPro 2023 (OriginLab). The inverse second-derivative of the absorbance spectra in the amide I region was calculated using a third-order Savitzky–Golay filter [6] with a 100–120-point window, depending on the data set. The inverse second derivative was baseline-corrected assuming flat baseline segments connecting minima between 1710 and 1595 cm^{-1}. The curves for each sample were then fit using the same starting parameters of 7 Gaussians centered at 1614, 1632, 1643, 1653, 1667, 1680, and 1692 cm^{-1}, corresponding to aggregated β-strands, β-sheets, random coil, α-helix, 3_{10} helix, β-turn, and parallel β-sheet structures, respectively. The insulin fibrils were fit with peaks starting at 1625, 1667, and 1680 cm^{-1}, corresponding to aggregated β-strands, 3_{10} helix, β-turn, respectively.

Insulin fibril preparation

To generate the insulin fibril samples, lyophilized bovine insulin (Cell Applications 128100) was dissolved in 20% acetic acid and the concentration was adjusted to 2 mM. The samples were then incubated at 68°C overnight as previously described [7,8]. For microscopy, the slide was assembled as described above, using double-sided tape, and sealing of the sample with mineral oil. The slide was then incubated on top of a heat block set to 75°C using Eppendorf lids as offsets to prevent direct contact with the block. The slide temperature was measured at 70°C using an infrared thermometer. The slide was incubated in the dark overnight.

Deep Etch Electron Microscopy

Samples for freeze-fracture were prepared by exchanging into 20 mM HEPES pH 7 as described above. The concentration of allY^{30GtoS} was adjusted for the final concentration to be 400-600 μM. NaCl was added to a final concentration of 150 mM to induce phase separation. The sample was then applied to a mica disk and either flash frozen immediately in liquid nitrogen or incubated overnight in a vapor chamber to allow the sample to age before flash freezing in nitrogen.

Replicas of deep etched samples for TEM were produced using a Leica EM ACE900 Freeze Fracture System. In brief, aged mica sandwiches were frozen by plunging into liquid nitrogen, separated beneath the surface of liquid nitrogen, and transferred to the ACE900 Freeze Fracture System. Then, water was sublimated at -80 °C for 1 hr, prior to shadowing with 7 nm Pt/C at an angle of 24°. The replica was supported by 8 nm carbon deposition at 85° before being washed through several DI water rinses and transferred to a copper TEM grid for TEM imaging (JEOL JEM-1400 Plus) at 120 kV.

Calculation of the complex shear modulus from video particle tracking microrheology of allY^{30GtoS} condensates

Since the motion of embedded particles within a fluid is driven by the thermal fluctuations of the fluid itself, the viscoelastic properties of the fluid can be estimated by analyzing the mean squared displacement (MSD) of the embedded probe particles. We do this by first calculating the fluid compliance from the MSD using [9]:

$$J(t) = \frac{3\pi a}{N_d k_B T} \langle \Delta r^2(\tau) \rangle \tag{1}$$

Here, a is the particle radius, N_d is the dimensionality of the probe particle motion (N_d=2 in our case), k_B is the Boltzmann constant, and T is the absolute temperature. Since the relaxation modulus $G(t)$ can be related to the compliance $J(t)$ by a convolution integral

$$\int_0^\tau G(t)J(\tau - t)dt = \tau, \tag{2}$$

the complex shear modulus can then be calculated using a Fourier transform as follows:

$$G^*(\omega) = \frac{1}{i\omega \hat{J}(\omega)} \tag{3}$$

where $\hat{J}(\omega)$ is the compliance in the Fourier space. We used two methods, one proposed by Evans et al., [10] and the other by Mason et al., [11] to convert the time-space compliance to frequency-space shear modulus $G^*(\omega)$.

In the method of Evans et al., the complex shear modulus $G^*(\omega)$ can be computed using:

$$\frac{i\omega}{G^*(\omega)} = i\omega J(0) + \frac{\left(1 - e^{-i\omega t_1}\right)\left(J_1 - J(0)\right)}{t_1} + \frac{e^{-i\omega t_N}}{\eta} + \sum_{k=2}^{N}\left(\frac{J_k - J_{k-1}}{t_k - t_{k-1}}\right)\left(e^{-i\omega t_{k-1}} - e^{-i\omega t_k}\right) \quad (4)$$

where (t_i, J_i) are the discrete experimental data points of the calculated compliance. The advantage of using the method of Evans et al.,[10] is that there is no fitting required of the data. This distinguishes it from the method of Mason et al., [11] where power law fitting is needed to convert the MSD to the rheological moduli. To improve the calculation, we oversampled the MSD data from our VPT measurements on AllY^{30GtoS} at different observation times (Main text **Fig. 3f**) using a cubic spline (**Supplementary Fig. S2**). The value of $J(0)$ was estimated by extrapolating the experimental data to $t = 0$ by a linear fit of the first four data points. Further, the value of η was estimated by a linear fit of the last ten points (using $\eta = 1/\dot{J}(t)$).

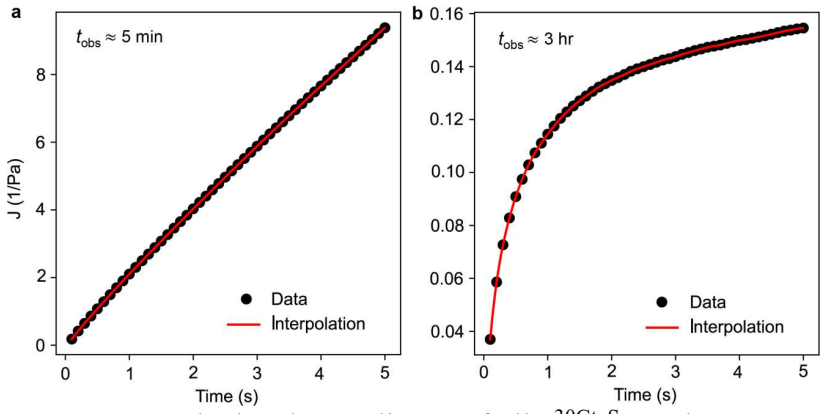

Supplementary Figure S2. Calculated compliance of allY^{30GtoS} condensates at (**a**) $t_{obs} \approx 5$ min and (**b**) $t_{obs} \approx 3$ hrs. Also plotted are the oversampled compliance functions (red) using a cubic spline. The compliance is calculated directly from the MSD data shown in **Fig. 3f** in the main text using equation 11.

The computation of the complex shear modulus can also be independently performed using the method of Mason et al.[11], which involves approximating the creep compliance as a power function.

$$J(t) = J_0 t^{\alpha} \quad (5)$$

where α is the diffusivity parameter which provides information on the nature of the diffusion process with $\alpha = 1$ representing normal Brownian diffusion and $\alpha < 1$ signifying a sub-diffusive process.

To estimate the complex shear modulus $G^*(\omega)$, the interpolated creep compliance (**Supplementary Fig. S2**) above was fitted locally to a power function. The neighbors in the local fit were weighted using a Gaussian function as described previously [11]. The fitting provides α at $\omega = 1/t$ that can be used to compute the complex shear modulus at frequencies $\omega = 1/t$ using [12]

$$G^*(\omega) = \frac{e^{i\pi\alpha/2}}{J\left(t = \frac{1}{\omega}\right)\Gamma(1+\alpha)} \tag{6}$$

where Γ is the gamma function.

Upon converting compliance data to complex moduli, using the methods of Evans et al., [10] as well as Mason et al., [11] we observe that allY^{30GtoS} condensates are dominantly viscous at $t_{obs} \approx$ 5 min (**Extended Data Fig. 5a-5c**). However, the elastic modulus of these condensates increases dramatically upon physical aging ($t_{obs} \approx$ 3 hrs). The overall shapes of the frequency-dependent viscoelastic moduli of aged allY^{30GtoS} condensates resemble that of Kelvin-Voigt solids (**Extended Data Figs. 5d, 5e**). Both methods yield consistent results (**Extended Data Fig. 5c, 5f**), confirming that allY^{30GtoS} condensates are dominantly elastic at long observation times ($t_{obs} \geq$ 3 hrs).

Supplementary Discussion

Note 1: The stickers-and-spacers framework for describing the phase behavior of PLCDs

Physical aging of protein condensates describes time-dependent changes in condensate material properties. Prior literature reports indicated a glass-type transition accompanying condensate aging [13]. In this model, the material properties of condensates at all ages are those of dominantly viscous, albeit dynamically frozen liquids. Glasses are disordered systems and glassy behaviors, which represent a loss of ergodicity [14] and mobility of molecules, have been attributed [13] to the ruggedness of free energy landscapes as captured by the random energy model [15]. The second form of aging is associated with the conversion of disordered fluids to ordered solids [16-18]. The morphologies of ordered solids are typically gleaned from a combination of structural analyses [19-21], mobility measurements, and measurements of increased fluorescence of molecular rotors such as thioflavin T (ThT).

Understanding the physical connection between sequence-encoded interactions and the time-dependent material properties necessitates a conceptual framework. The stickers-and-spacers framework [22] has been useful for modeling and explaining the origins of sequence-specific driving forces for condensate formation by PLCDs [1,2,23]. Aromatic residues are stickers that form reversible physical crosslinks [1,2,23]. Spacers in PLCDs are primarily Gly, Ser, Asn, and Gln residues. They affect overall solubility while influencing the coupling between phase separation and percolation [1,2,23]. Recent lattice-based coarse-grained simulations reproduced the measured phase behaviors for thirty different variants of A1-LCD [23], the PLCD derived from the RNA binding protein hnRNP A1. These computations showed that A1-LCD and designed variants form physically crosslinked networks within condensates. The network organization was found to have hub-and-spoke-like structures. Multimolecular hubs are defined by the extent of intermolecular physical crosslinking mediated by aromatic stickers, and the spokes are governed by spacer-mediated transport of molecules between hubs, which also requires the breaking of crosslinks [23,24]. The interplay between sticker- and spacer-mediated effects leads to the spatially inhomogeneous organization of A1-LCD and related molecules. Overall, the present work provides a quantitative assessment of the role of sticker and spacer residues in proteins to regulate condensate viscoelasticity and aging.

Note 2: Connections between condensate structure and moduli

Our quantifications of moduli, which are based on simulated structures of condensates, use a graph-theoretic adaptation [25,26] of the Rouse-Zimm theory [27,28] for polymer dynamics. The standard implementation of Rouse-Zimm theory is a bead-and-spring model for the dynamics of a single chain [27,28]. Key ingredients are: (i) the friction of the medium; (ii) the mobility tensor, including contributions from hydrodynamic interactions; (iii) the Zimm matrix whose elements are determined by the specific interactions of the chain; and (iv) the stochastic contributions due to Brownian motion. Since our focus is on the contributions of equilibrium internal structures of condensates to their viscoelastic moduli, we adopted a simplification of the Rouse-Zimm theory due to Peticolas[29] and focused on the eigenvalue spectrum of the Zimm matrix, which is equivalent to a graph Laplacian [30]. This approach is useful because the solvent is implicit in our simulations, meaning that our Zimm matrices do not account for hydrodynamic interactions.

The spectrum of eigenvalues defines the relaxation times due to interconversions of the network defined by molecules that are physically crosslinked. Using the standard formulation of Rouse-Zimm theory, the graph for a given chain conformation is defined by nodes representing

the residues in the chain, and the edges connecting nodes indicate physical contact between two residues on the lattice. The diagonal elements of the resulting Zimm matrices indicate the degree, defined as the number of edges incident on a node, where a node is a residue in a chain. The off-diagonal elements specify the connectivity. These are set to –1 if there is an edge between two nodes or 0 if there is no edge. From the published simulations [23], we extracted ensembles of condensate-specific graph Laplacians and computed their eigenvalue spectra, which are the relaxation times. The Fourier transform of the superposition of relaxation times shows that the simulated condensates have frequency-dependent storage and loss moduli with a single, system-specific crossover frequency. To put the computed moduli on the same scale as the measurements, we scaled the computed crossover frequency to match experimentally derived values. No other information from the experiment was used in comparing computations to experiments.

Are the dynamics of a single chain in an effective solvent sufficient for explaining measured viscoelastic moduli of A1-LCD-based condensates, or must one account for the sequence-specific network structures within condensates? We answered this question by comparing measured and computed complex moduli for condensates formed by WT^{+NLS}. For the computations, we used two versions of the Zimm matrix namely, the "single-chain model" and the "collective model". In the "single-chain model", the nodes represent residues on a single chain within the condensate, and the edges are defined by bonded and non-bonded intra-chain contacts. The Zimm matrix was calculated as $\boldsymbol{Z} = \boldsymbol{BWB}^T$ where the unoriented incidence matrix $\boldsymbol{B}$ has elements B_{ij} and the matrix $\boldsymbol{W}$ is the matrix of edge weights. For $j \neq i$, the elements B_{ij} are set to 1 if there is a node i incident upon edge j; otherwise, B_{ij} equals zero [30]. For n nodes and m edges, the incidence matrix has size $n \times m$. The $m \times m$ weight matrix is square and it has Boltzmann-weighted residue-residue interaction energies [23] along the diagonal and zero otherwise. For the "collective model", we calculated the Zimm matrices from a graph where the nodes are individual chains, and the edges define any inter-residue contacts between chains with no further weighting. In this model, the collection of molecules in the condensate-spanning network are modeled as a single chain.

We find that the equilibrium ensemble-averaged properties of condensates contain most of the information that enables reproduction of measured moduli. The only adjustable parameter is the value of the crossover frequency, which we fix using measured values. For condensates formed by WT^{+NLS}, the moduli computed using the collective model show good agreement with the measured moduli (**Fig. 1b; Extended Data Fig. 1d, 1e**). This stands in contrast to the single-chain model (**Extended Data Fig. 1f**), which does a poor job of reproducing measured moduli, especially the storage moduli. This is true irrespective of whether we edge-weight the Zimm matrix (**Extended Data Fig. 1g**). The difference between the plots using the weighted and unweighted Zimm matrices obtained using the single-chain model is negligible. Together, these results suggest that the moduli, especially the storage modulus, are governed by details of network structures that define how the WT^{+NLS} molecules are organized within the condensate. Based on our results, viscoelastic moduli appear to be collective properties, which are defined by the network of intra- and intermolecular interactions. This seems to be the case for the storage moduli in particular. These properties cannot be captured fully by probing the motions of a single chain [31]. Instead, the network of molecules becomes an effective single chain in our instantiation of the Rouse-Zimm model that reproduces measured moduli.

Finally, in our pMOT experiments, the presence of a single crossover frequency and the specific functional forms we extract for the frequency dependencies above and below $\omega_{crossover}$

imply that WT^{+NLS} condensates probed at $t_{obs} \approx 5$ min are viscoelastic Maxwell fluids [13,32]. The apparent deviations from Maxwell-like behaviors at low frequencies (**Fig. 1b**) are likely due to unavoidable noise in the long-time position autocorrelation functions measured using pMOT. We also note that the computed moduli of the allF variant are characteristic of a Maxwell fluid with a single crossover frequency (**Extended Data Fig. 2a**). The crossover cannot be gleaned from the experimental data alone. Experimentally, the inferred increase in $\omega_{crossover}$ is substantial, thus preventing its direct measurement using pMOT (**Fig. 1d**). Taken together, we find that $\omega_{crossover}$ changes by three orders of magnitude for condensates formed by A1 LCD variants, being the highest for allF and lowest for allW. Crossover to predominantly elastic regimes occurs at frequencies that are sequence-specific and encoded by sticker valence and strength.

Note 3: A technical note on the LaSSI model

The LaSSI model used in this work employs a learning paradigm as opposed to a one-size-fits-all transferrable model. Specifically, we use a Gaussian process Bayesian optimization approach [33], which for single component systems leverages available experimental data such as small-angle X-ray scattering data [1] for the single chains in the one-phase regime [23]. Alternatively, atomistic simulations of the R_g distributions with Tyr-to-Trp and Phe-to-Trp substitutions will suffice. However, at this juncture, neither input is available because of the ultra-low saturation concentrations associated with systems featuring multiple Trp residues. Absent a reliable parameterization of the interactions involving Trp residues, we were not able to perform LaSSI simulations for variants where Phe and Tyr residues are replaced with Trp. Our preliminary simulations based on polarizable models suggest that Trp, as a sticker, has an effective valence that is greater than one [34]. This hypothesis, which explains why Trp, like other systems with five- and six-membered rings such as purine nucleobases [35,36] make for stronger stickers than Tyr and Phe, will need systematic measurements of thermodynamic parameters and additional calibrations.

Note 4: On the correlation between bulk viscosity and saturation concentration

We used computations to quantify the temperature dependence of viscosities within A1-LCD condensates. These viscosities were computed by tracking the timescale associated with the motions of the centers of mass of the molecules within condensates. For all sequences studied to date, the concentrations in condensates of A1-LCD and variants thereof change minimally with temperature except near the critical temperature [1]. Accordingly, the temperature-dependent saturation concentrations (c_{sat}) can be used to quantify the free energy change associated with transferring A1-LCDs and designed sequence variants across the temperature- and variant-specific phase boundary [1].

Is there a connection between temperature-dependent intra-condensate viscosities and c_{sat} values? Computations reveal (Fig. 2) a strong one-to-one correspondence between bulk viscosity within condensates and c_{sat}, which quantifies the driving forces for phase separation. We observed that all the data collapse onto a single master curve (Fig. 2a) without requiring any adjustable parameters or fitting. This shows a clear and strong one-to-one correspondence between viscosity and c_{sat} and suggests an apparent universality as opposed to system-specificity. Note that these data also include computed results for the PLCD from the protein Fused in Sarcoma (FUS).

We next experimentally quantified the strength of the correlation between dynamical bulk viscosity and c_{sat} and compared those results with our computational results. We measured mean squared displacements (MSDs) of probe particles within A1-LCD-based condensates using video particle tracking (VPT) at variable temperatures (**Extended Data Fig. 3a**). The VPT measurements allow us to monitor the motions of 200 nm probe particles in condensates for longer timescales (hundreds of seconds) and over longer distances that are not constrained by the optical trap. This enabled the measurement of viscosities at longer timescales, with improved statistics afforded by being able to track tens to hundreds of independent probe particles (**Extended Data Fig. 3b**). For each of the seven variants, our experiments show maintenance of the one-to-one correspondence between viscosity and c_{sat} (**Fig. 2b**) with Pearson *r*-values akin to those we estimate from computations. However, instead of the data collapsing onto a single master curve, we find system-specific inverse correlations between viscosity and c_{sat}. This is not due to discrepancies between computed and measured c_{sat} values, because these are essentially identical to one another [23]. Instead, the variant-specific slopes and intercepts in the measurements are attributable to hydrodynamic effects within condensates, which are not included in the simulations and are likely the result of correlations between solvent-mediated, system-specific interactions in condensates.

The differences between computations and measurements allow us to quantify the magnitudes of hydrodynamic contributions using a method of comparative slopes. Here, we denote m_0 to be the slope of the master curve derived from the plot of ln(viscosity) versus ln(c_{sat}) using computations. Next, we denote m_i as the slope for variant i derived using system-specific measurements. The ratio $s_i = (m_i / m_0)$ quantifies the contribution from hydrodynamics for variant i. A value of s_i that is less than unity implies that hydrodynamic interactions weaken the correspondence between the dynamical properties of condensates and the free energy of transfer between dilute and dense phases. A value of s_i that is greater than unity implies that a favorable transfer free energy from dilute to dense phases (lower c_{sat} values) is amplified by intra-condensate hydrodynamic interactions. From comparisons of measurements and computations, we find that the s_i values are 0.7, 1.5, and 1.9, for allY, allF, and WT^{+NLS}, respectively. The implication is that hydrodynamic and thermodynamic effects show negative cooperativity for allY and positive cooperativity for allF and WT^{+NLS}. These effects do not follow the hierarchy of sticker-sticker interactions. Instead, they appear to be governed by a system-specific interplay of solvent-chain, and chain-chain interactions within condensates whereby variants with higher relative Phe or Trp contents show steeper slopes, while variants with higher Tyr contents exhibit shallower slopes.

Recently, coarse-grained molecular dynamics simulations have established a one-to-one correspondence between the radii of gyration (R_g) of disordered proteins in dilute phases and the viscosities in condensates [37]. There is also a well-established positive, one-to-one correspondence between c_{sat} values and dilute phase R_g values [1,2,23,38]. Clearly, computations based on coarse-grained models predict a strong, master-curve-like one-to-one correspondence between viscosity and c_{sat}. However, while the strong negative correlation is preserved in the experiments, the quantitative one-to-one correspondence is system-specific. Simulations and theories to explain this observation are currently unavailable. Our findings provide the impetus for further explorations of the origins of the system-specificity of hydrodynamic interactions.

For a given temperature, viscosities quantify the frictional effects that arise due to the molecular and mesoscale interactions among molecules and these interactions are solvent-mediated. The temperature dependence of viscosity quantifies the energy barrier to reconfiguration of the network of crosslinked molecules. This can be extracted using thermorheology [39,40]. These

barriers are referred to as flow activation energies because they represent the thermal energy required to overcome the barrier to enable the flow of molecules. To quantify flow activation energies, we measured MSDs of probe particles within A1-LCD-based condensates using VPT as a function of temperature. This allowed us to derive temperature dependencies of viscosities of different condensates (**Extended Data Figs. 3c, 3d**). The measured temperature dependence of condensate viscosities conforms to an Arrhenius relationship (**Extended Data Fig. 3e**) [40,41], which was also observed in our computational results (**Extended Data Fig. 3f**). The Arrhenius relationship highlights the presence of a single, system-specific barrier to network reconfiguration.

From fits to the Arrhenius relationships, we extracted flow activation energies using data from measurements and computations in units of RT, where $T = 25^{\circ}C$ is the reference temperature, and R is the ideal gas constant. We compared the magnitudes of the flow activation energies derived from computations (**Fig. 2c** and **Extended Data Fig. 3g**) to those derived from VPT measurements (**Fig. 2d**). To enable the comparisons, we call the computed barrier for condensates formed by sequence i as $E_{F,0i}$. The computed values do not account for hydrodynamic effects. Instead, they quantify the contributions of network structures that form within condensates and are system-specific. We find that the computed barriers for condensates are distributed between 26 RT and 32 RT (**Fig. 2c**, **Extended Data Fig. 3g**). These values reflect the extent of crosslinking within simulated condensates [23]. As shown previously, the extent of crosslinking does not correlate strongly with c_{sat} [23]. This is true of the computed values of $E_{F,0i}$ as well.

If we denote $E_{F,i}$ (**Fig. 2d**) as the measured flow activation energy for system i, we can compute the ratio $E_F' = (E_{F,i} / E_{F,0i})$. This allows the estimation of sequence-specific hydrodynamic contributions to the flow activation energy that are missing in the lattice simulations. If E_F' equals unity, there are negligible contributions from hydrodynamic effects to the energy barrier for network reconfiguration. Conversely, if E_F' is less than unity, then hydrodynamic effects lower the barrier, and the opposite is true if E_F' is greater than unity. From comparisons of measurements and computations, we find that the E_F' values are ≈ 1.1, 1.4, and 1.6 for allY, allF, and WT^{+NLS}, respectively. This indicates a minor role of hydrodynamic effects in determining the flow activation barrier for allY condensates. However, hydrodynamic effects increase the barriers for condensates formed by allF and WT^{+NLS}. Taken together with the comparative slope analysis, we find that there is negative cooperativity between hydrodynamic effects and the strengths of intermolecular interactions in determining the viscosity of allY condensates. However, the barrier to flow activation is minimally affected by hydrodynamic effects. For the allF and WT^{+NLS} condensates, there is positive cooperativity between hydrodynamic effects and the strengths of intermolecular interactions as determinants of bulk condensate viscosity, and an enhancement of the barrier to network reconfiguration by hydrodynamic effects.

Note 5: On the mechanism and regulation of condensate physical aging

Previous studies showed that the replacement of Gly residues with Ser weakens the driving forces for condensation of A1-LCD-based systems [1]. This effect could be explained by the higher effective solvation volume of Ser over Gly [42]. However, the extent of internal crosslinking within condensates, which is governed by the associativity of multivalent macromolecules [43], does not have to follow the driving forces for phase separation, which are driven by solubility considerations. Our VPT-based microrheology measurements revealed that WT^{30GtoS} condensates, which are highly dynamic at early time points as seen by the motion of embedded 200 nm

polystyrene particles, become dynamically arrested within t_{obs} < 10 min. This accelerated aging prevented quantitative measurements of viscosity and viscoelastic properties of WT^{30GtoS} condensates. However, the same spacer mutations in the allY variant showed dynamical arrest at a slower timescale (~ 1.5 hrs), allowing us to probe the nature of this dynamical arrest in greater detail. For $t_{obs} \approx 5$ min, the particles within $allY^{30GtoS}$ condensates showed diffusive behavior as expected for a material that behaves as a viscous fluid at long timescales. However, after $t_{obs} \approx 3$ hr, the measured MSD profiles were sublinear (**Fig. 3f**). The flatness of the MSD curves at longer lag-times and the histogram of RMSDs, which initially showed a peak around an RMSD of ~0.25 μm, showed a sharp peak near zero within 3 hours indicate a complete dynamical arrest of the condensate (**Fig. 3d, bottom**).

Taken together, the picture that emerges is as follows: Gly-to-Ser substitutions on a common allY background of stickers weaken the driving forces for condensate formation. Viscosities of condensates observed at $t_{obs} \approx 5$ min are lowered with an increased number of Gly-to-Ser substitutions. However, because the sticker valence remains the same as in the allY system, the extent of crosslinking within condensates remains high. Therefore, the Gly-to-Ser substitutions show a combination of high early-time mobility and high degrees of crosslinking. This combination leads to unexpected behaviors such as the onset of dynamical arrest and accelerated physical aging of the dense phase. Notably, the timescales for complete dynamical arrest decrease with increasing numbers of Gly to Ser substitutions, highlighting the programmability of dynamical arrest through mutations to spacers (**Fig. 3d**).

What may be the physical origin of accelerated dynamical arrest caused by Gly-to-Ser substitutions? Increasing the number of Gly-to-Ser substitutions increases the compliance of networks formed within condensates that are dominantly viscous (**Fig. 3g**). This was inferred from simulation results. Furthermore, viscoelastic moduli inferred from VPT-based microrheology (Fig. 5) reveal a transition from a dominantly viscous state to an elastic state upon dynamical arrest. Specifically, the loss modulus is an order of magnitude higher than the storage modulus within the experimental frequency range (~0.1 to 10 Hz). The elastic modulus is on the order of ~0.01 Pa, and its rapid fluctuation reflects the noise of the MSD measurement at long lag times where the time-averaged statistics are much lower than for short lag times. Importantly, we find that, upon physical aging, the elastic modulus increases dramatically for condensates of $allY^{30GtoS}$, which are dynamically arrested at $t_{obs} \approx 3$ hrs. We also directly tested the dominant elastic response of aged condensates formed by $allY^{20GtoS}$ using optical tweezer-based creep tests. In a dominantly elastic material, local motions of an optically-tapped particle at short timescales are allowed whereas, at longer timescales, the particle is constrained within physical cages that are set up by elastic networks that form on system-specific length scales [44]. Our experiments (**Fig. 4** and **Extended Data Fig. 6**) revealed that the probe particle was lost from the optical trap at ~1 μm. Upon being lost from the trap, the probe particle recoiled back to its original position as expected for a Kelvin-Voigt solid. Taken together with the viscoelastic moduli estimated using MSD data (**Extended Data Figs. 5g, 5h, 5i)**, we conclude that physically aged condensates are dominantly elastic solids. Note that aging was promoted by mutations to spacers, and hence the extent of crosslinking between different condensates should not change. However, the spacer-mediated compliance of the networks can change, and this enables facile transitions to dominantly elastic materials.

The free energy profiles in **Fig. 7** are annotated by two features. The fluid and elastic solid phases are represented using a standard linear solid or Zener model [45]. In this model, a time-dependent rise of the elasticity of the E1 element captures the transitions from a dominant

Maxwell-type behavior of nascent condensates ($E1 < E_2$) to a Kelvin-Voigt-type behavior as condensates age ($E1 >> E_2$). We also allow for the possibility that increased metastability of the fluid state arises from ruggedness within the well that corresponds to low values of Φ. Our proposal represents a combination of the Landau picture [46] of phase transitions along ($\Phi \mid c_{dense}$) and the Zwanzig picture [47] of roughness within the disordered fluid phase.

Overall, our experimental data and computational results are concordant with terminally viscous fluid-like states of A1-LCD condensates being metastable, disordered phases. Disorder-to-order transitions enable conversion from metastable fluids to globally stable solids. Interestingly, in the absence of mutations to spacers, the activation barriers for network reconfiguration of fluid-like phases can be prohibitive, being on the order of 30 *RT* or twice as large depending on the sticker identities. This suggests that naturally occurring sticker and spacer grammars ensure enhanced metastability of A1-LCD-based and possibly other PLCD condensates. This might explain why fluid phases are so readily observed in live cells, and why considerable attention has focused on the functional relevance of fluid forms of condensates.

Our findings on the terminally elastic state of the A1-LCD aged condensates and the resultant proposals are distinct from those of Jawerth et al. They used active microrheology and fluorescence recovery after photobleaching to characterize condensates formed by the protein PGL3 [13]. Jawerth et al. found that fluid-like condensates formed by this protein are Maxwell fluids, a result we recapitulate for A1-LCD-based condensates. They also found that aged condensates continue to behave as Maxwell fluids, even though the condensates no longer fused, and rheology measurements suggested that the condensates were dynamically arrested upon aging. Based on their observations, Jawerth et al. proposed that the PGL3 condensates were "Maxwell glasses" defined as Maxwell fluids showing age-dependent terminal relaxation times [13]. Our data, based on direct measurements of dominant states, leads to a different picture for A1-LCD condensates. We propose that viscoelastic Maxwell fluids are metastable. Weakening the metastability of terminally viscous states unmasks the transition to a globally stable, dominantly elastic state, which for the A1-LCD-based systems appears to be a Kelvin-Voigt, non-fibrillar solid.

Recent bioinformatics analyses showed an inverse correlation between sticker and spacer identities [1]. Increasing the number of Tyr stickers is positively correlated with increased numbers of Gly residues as spacers. In contrast, increased numbers of Phe stickers are accompanied by increased number of Ser residues as spacers. Measurements of PLCDs that form solids in cellular systems have also documented a preference for high numbers of Phe stickers and Ser residues as spacers [48]. Taken together, these trends suggest an evolutionarily encoded preference whereby there is either a selection for enhanced metastability of fluid-like phases (positive correlation between Tyr and Gly contents) or a selection for facile transitions to solid phases (positive correlation between Phe and Ser contents). How this plays out for condensates formed by mixtures of PLCDs with compositionally distinct preferences will need further investigation [24]. Importantly, being able to compute moduli from simulations of the network structures of condensates [23] should allow us to design PLCD sequences with bespoke material properties [24,49].

Previous work showed that the linear patterning of aromatic stickers affects the formation of fluid- versus solid-like PLCD condensates [2,50]. In full-length proteins with PLCDs, Wang et al. showed that mutations to spacers can have a direct impact on the time-dependent changes to mobilities in dense phases [51]. Given the large barriers we estimate for network rearrangements (**Fig. 2c, 2d**), it appears that for many naturally occurring systems, including PLCDs, the barrier to conversion from metastable viscous fluids to globally stable elastic solids might be

insurmountable on biologically relevant timescales, especially for those that are turned over rapidly. This might explain why "dynamicity" is often invoked as a key determinant of condensate functions in cells [52-54]. In contrast to condensates that turn over, there are long-lived condensates such as Balbiani bodies [55], where the sticker grammars and choice of spacers appear to enable facile conversion to dominantly elastic solid phases [50]. Likewise, the sequence grammars of scaffolds of solid phase condensates such as A-bodies in nuclei of stressed cells [56] might be such that the barriers to conversion from fluids to solids are readily negotiated on functionally relevant timescales. Our work highlights the importance of connections between sequence-encoded interactions and the time-dependent material properties of condensate-forming systems. Our work also invites detailed structural characterizations of metastable fluids and globally stable solid phases, to investigate how the interplay of homotypic and heterotypic interactions influence material states and structures in multicomponent mixtures [24,57-59].

Supplementary Tables

Table S1: Amino acid sequences of the variants used in pMOT and VPT measurements.

[a]	Protein sequence[b]	[c]
allF	GSMASASSSQRGRSGSGN**F**GGGRGGG**F**GGNDN**F**GRGGN**F**SGRGG**F**GGSRGGGG**F**GGS GDG**F**NG**F**GNDGSN**F**GGGGS**F**ND**F**GN**F**NNQSSN**F**GPMKGGN**F**GGRSSGGSGGGGQ**FF**A KPRNQGG**F**GGSSSSSS**F**GSGRR**F**	19F
WT	GSMASASSSQRGRSGSGN**F**GGGRGGG**F**GGNDN**F**GRGGN**F**SGRGG**F**GGSRGGGG**Y**GGS GDG**Y**NG**F**GNDGSN**F**GGGGS**Y**ND**F**GN**Y**NNQSSN**F**GPMKGGN**F**GGRSSGP**Y**GGGGQ**Y F**A KPRNQGG**Y**GGSSSSSS**Y**GSGRR**F**	8Y 12F
allY	GSMASASSSQRGRSGSGN**Y**GGGRGGG**Y**GGNDN**Y**GRGGN**Y**SGRGG**Y**GGSRGGGG**Y**GGS GDG**Y**NG**Y**GNDGSN**Y**GGGGS**Y**ND**Y**GN**Y**NNQSSN**Y**GPMKGGN**Y**GGRSSGGSGGGGQ**YY**A KPRNQGG**Y**GGSSSSSS**Y**GSGRR**Y**	19Y
W-	GSMASASSSQRGRSGSGNSGGGRGGG**W**GGNDN**W**GRGGNSSGRGG**W**GGSRGGGG**W**GGS GDG**W**NG**W**GNDGSNSGGGGSSND**W**GN**W**NNQSSN**W**GPMKGGN**W**GGRSSGGSGGGGQ**W**SA KPRNQGG**W**GGSSSSSSSGSGRR**W**	13W
YtoW	GSMASASSSQRGRSGSGN**F**GGGRGGG**F**GGNDN**F**GRGGN**F**SGRGG**F**GGSRGGGG**W**GGS GDG**W**NG**F**GNDGSN**F**GGGGS**W**ND**F**GN**W**NNQSSN**F**GPMKGGN**F**GGRSSGSGGGGGQ**W F**A KPRNQGG**W**GGSSSSSS**W**GSGRR**F**	7W 12F
FtoW	GSMASASSSQRGRSGSGN**W**GGGRGGG**W**GGNDN**W**GRGGN**W**SGRGG**W**GGSRGGGG**Y**GGS GDG**Y**NG**W**GNDGSN**W**GGGGS**Y**ND**W**GN**Y**NNQSSN**W**GPMKGGN**W**GGRSSGSGGGGGQ**Y W**A KPRNQGG**Y**GGSSSSSS**Y**GSGRR**W**	12W 7Y
allW	GSMASASSSQRGRSGSGN**W**GGGRGGG**W**GGNDN**W**GRGGN**W**SGRGG**W**GGSRGGGG**W**GGS GDG**W**NG**W**GNDGSN**W**GGGGS**W**ND**W**GN**W**NNQSSN**W**GPMKGGN**W**GGRSSGSGGGGGQ**WW**A KPRNQGG**W**GGSSSSSS**W**GSGRR**W**	19W
WT^{20GtoS}	GSMASASSSQR**S**RSGSGN**F S**G**S**R**S**G**S**F S**GNDN**F**GR**S**GN**F**SGR**S**G**F**GGSR**S**GGG**Y S**GS GD**S Y**NS**F**GNDGSN**F S**G**S**GS**Y**ND**F**GN**Y**NNQSSN**F**GPMK**S**GN**F**GGRSSGSSGG**S**GQ**Y F**A KPRNQG**S Y S**GSSSSSS**Y**GS**S**RR**F**	7Y 12F
WT^{30GtoS}	GSMASASSSQR**S**RS**S**SGN**F S**G**S**R**S**G**S**F S**GNDN**F**GR**S**GN**F**SGR**S**G**F S**GSR**S**G**S**G**Y S**GS **S**D**S Y**N**S F**GND**S**SN**F S**G**SS**S**Y**ND**F**GN**Y**NNQSSN**F**GPMK**S**GN**F S**GRSS**S**SSG**SS**GQ**Y F**A KPRNQG**S Y S**GSSSSSS**Y S S**RR**F**	7Y 12F
allY^{20GtoS}	GSMASASSSQR**S**RSGSGN**Y S**G**S**R**S**G**S Y S**GNDN**Y**GR**S**GN**Y**SGR**S**G**Y**GGSR**S**GGG**Y S**GS GD**S Y**NS**Y**GNDGSN**Y S**G**S**GS**Y**ND**Y**GN**Y**NNQSSN**Y**GPMK**S**GN**Y**GGRSSGSSGG**S**GQ**YY**A KPRNQG**S Y S**GSSSSSS**Y**GS**S**RR**Y**	19Y
allY^{30GtoS}	GSMASASSSQR**S**RS**S**SGN**Y S**G**S**R**S**G**S Y S**GNDN**Y**GR**S**GN**Y**SGR**S**G**Y S**GSR**S**G**S**G**Y S**GS **S**D**S Y**N**S Y**GND**S**SN**Y S**G**SS**S**Y**ND**Y**GN**Y**NNQSSN**Y**GPMK**S**GN**Y S**GRSS**S**SSG**SS**GQ**YY**A KPRNQG**S Y S**GSSSSSS**Y S S**RR**Y**	19Y

[a] variant name; [b] the N-terminal GS-extensions are leftovers of TEV cleavage sites; [c] number and type of aromatic residues in the sequence

Table S2: Amino acid sequences of the variants for which computations were performed and reported in Fig. 2a. The simulation results for these variants were taken from the work of Farag et al [23]. Following this work, simulations of FUS-LCD and of a homopolymer whose properties were tuned to give rise to phase behavior closely matching that of A1-LCD WT^{-NLS} [23] were also analyzed.

Construct	Amino acid sequence
WT^{-NLS}	GSMASASSSQRGRSGSGNFGGGRGGGFGGNDNFGRGGNFSGRGGFGGSRGGGGYGGSGDGY NGFGNDGSNFGGGGSYNDFGNYNNQSSNFGPMKGGNFGGRSSGGSGGGGQYFAKPRNQGGY GGSSSSSSYGSGRRF
WT^{+NLS}	GSMASASSSQRGRSGSGNFGGGRGGGFGGNDNFGRGGNFSGRGGFGGSRGGGGYGGSGDGY NGFGNDGSNFGGGGSYNDFGNYNNQSSNFGPMKGGNFGGRSSGPYGGGGQYFAKPRNQGGY GGSSSSSSYGSGRRF
-12F+12Y (allY)	GSMASASSSQRGRSGSGNYGGGRGGGYGGNDNYGRGGNYSGRGGYGGSRGGGGYGGSGDGY NGYGNDGSNYGGGGSYNDYGNYNNQSSNYGPMKGGNYGGRSSGGSGGGGQYYAKPRNQGGY GGSSSSSSYGSGRRY
+7F-7Y (allF)	GSMASASSSQRGRSGSGNFGGGRGGGFGGNDNFGRGGNFSGRGGFGGSRGGGGFGGSGDGF NGFGNDGSNFGGGGSFNDFGNFNNQSSNFGPMKGGNFGGRSSGGSGGGGQFFAKPRNQGGF GGSSSSSSFGSGRRF
-4F-2Y	GSMASASSSQRGRSGSGNSGGGRGGGFGGNDNFGRGGNSSGRGGFGGSRGGGGYGGSGDGY NGFGNDGSNSGGGGSSNDFGNYNNQSSNFGPMKGGNFGGRSSGGSGGGGQYSAKPRNQGGY GGSSSSSSSGSGRRF
-9F+6Y	GSMASASSSQRGRSGSGNFGGGRGGGYGGNDNYGRGGNYSGRGGFGGSRGGGGYGGSGDGY NGGGNDGSNYGGGGSYNDSGNYNNQSSNFGPMKGGNYGGRSSGGSGGGGQYGAKPRNQGGY GGSSSSSSYGSGRRY
-8F+4Y	GSMASASSSQRGRSGSGNFGGGRGGGYGGNDNGGRGGNYSGRGGFGGSRGGGGYGGSGDGY NGGGNDGSNYGGGGSYNDSGNYNNQSSNFGPMKGGNYGGRSSGGSGGGGQYGAKPRNQGGY GGSSSSSSYGSGRRF
-9F+3Y	GSMASASSSQRGRSGSGNFGGGRGGGYGGNDNGGRGGNYSGRGGFGGSRGGGGYGGSGDGY NGGGNDGSNYGGGGSYNDSGNGNNQSSNFGPMKGGNYGGRSSGGSGGGGQYGAKPRNQGGY GGSSSSSSYGSGRRS
+12D	GSMASADSSQRDRDDSGNFGDGRGGGFGGNDNFGRGGNFSDRGGFGGSRGDGGYGGDGDGY NGFGNDGSNFGGGGSYNDFGNYNNQSSNFDPMKGGNFGDRSSGPYDGGGQYFAKPRNQGGY GGSSSSSSYGSDRRF
+8D	GSMASASSSQRDRSGSGNFGGGRDGGFGGNDNFGRGDNFSGRGDFGGSRDGGGYGGSGDGY NGFGNDGSNFGGGGSYNDFGNYNNQSSNFGPMKGGNFGGRSSDPYGGGGQYFAKPRNQDGY GGSSSSSSYDSGRRF

+4D	GSMASASSSQRDRSGSGNFGGGRGGGFGGNDNFGRGGNFSGRGDFGGSRGGGGYGGSGDGY NGFGNDGSNFGGGGSYNDFGNYNNQSSNFGPMKGGNFGGRSSDPYGGGGQYFAKPRNQGGY GGSSSSSSYDSGRRF
-4D	GSMASASSSQRGRSGSGNFGGGRGGGFGGNGNFGRGGNFSGRGGFGGSRGGGGYGGSGGGY NGFGNSGSNFGGGGSYNGFGNYNNQSSNFGPMKGGNFGGRSSGPYGGGGQYFAKPRNQGGY GGSSSSSSYGSGRRF
+2R	GSMASASSSQRGRSGSGNFGGGRGGGFGGNDNFGRGGNFSGRGGFGGSRGGGGYGGSGDGY NGFRNDGSNFGGGGRYNDFGNYNNQSSNFGPMKGGNFGGRSSGPYGGGGQYFAKPRNQGGY GGSSSSSSYGSGRRF
-6R	GSMASASSSQGGRSGSGNFGGGRGGGFGGNDNFGGGGNFSGSGGFGGSRGGGGYGGSGDGY NGFGNDGSNFGGGGSYNDFGNYNNQSSNFGPMKGGNFGGSSSGPYGGGGQYFAKPGNQGGY GGSSSSSSYGSGGRF
-10R	GSMASASSSQGGSSGSGNFGGGGGGGFGGNDNFGGGGNFSGSGGFGGSGGGGGYGGSGDGY NGFGNDGSNFGGGGSYNDFGNYNNQSSNFGPMKGGNFGGSSSGPYGGGGQYFAKPGNQGGY GGSSSSSSYGSGGGF
-3R+3K	GSMASASSSQRGKSGSGNFGGGRGGGFGGNDNFGRGGNFSGRGGFGGSKGGGGYGGSGDGY NGFGNDGSNFGGGGSYNDFGNYNNQSSNFGPMKGGNFGGRSSGGSGGGGQYFAKPRNQGGY GGSSSSSSYGSGRKF
-6R+6K	GSMASASSSQKGKSGSGNFGGGRGGGFGGNDNFGKGGNFSGRGGFGGSKGGGGYGGSGDGY NGFGNDGSNFGGGGSYNDFGNYNNQSSNFGPMKGGNFGGKSSGGSGGGGQYFAKPRNQGGY GGSSSSSSYGSGRKF
+7K+12D	GSMASADSSQRDRDDKGNFGDGRGGGFGGNDNFGRGGNFSDRGGFGGSRGDGKYGGDGDKY NGFGNDGKNFGGGGSYNDFGNYNNQSSNFDPMKGGNFKDRSSGPYDKGGQYFAKPRNQGGY GGSSSSKSYGSDRRF
-20G+20S (WT^{20GtoS})	GSMASASSSQRSRSGSGNFSGSRSGSFSGNDNFGRSGNFSGRSGFGGSRSGGGYSGSGDSY NSFGNDGSNFSGSGSYNDFGNYNNQSSNFGPMKSGNFGGRSSGSSGGSGQYFAKPRNQGSY SGSSSSSSYGSSRRF
-30G+30S (WT^{30GtoS})	GSMASASSSQRSRSSSGNFSGSRSGSFSGNDNFGRSGNFSGRSGFSGSRSGSGYSGSSDSY NSFGNDSSNFSGSSSYNDFGNYNNQSSNFGPMKSGNFSGRSSSSSGSSGQYFAKPRNQGSY SGSSSSSSYSSSRRF
-12F+12Y-20G+20S ($allY^{20GtoS}$)	GSMASASSSQRSRSGSGNYSGSRSGSYSGNDNYGRSGNYSGRSGYGGSRSGGGYSGSGDSY NSYGNDGSNYSGSGSYNDYGNYNNQSSNYGPMKSGNYGGRSSGSSGGSGQYYAKPRNQGSY SGSSSSSSYGSSRRY
-12F+12Y-30G+30S ($allY^{30GtoS}$)	GSMASASSSQRSRSSSGNYSGSRSGSYSGNDNYGRSGNYSGRSGYSGSRSGSGYSGSSDSY NSYGNDSSNYSGSSSYNDYGNYNNQSSNYGPMKSGNYSGRSSSSSGSSGQYYAKPRNQGSY SGSSSSSSYSSSRRY

+7F-7Y-20G+20S ($allF^{20GtoS}$)	GSMASASSSQRSRSGSGNFSGSRSGSFSGNDNFGRSGNFSGRSGFGGSRSGGGFSGSGDSF NSFGNDGSNFSGSGSFNDFGNFNNQSSNFGPMKSGNFGGRSSGSSGGSGQFFAKPRNQGSF SGSSSSSSFGSSRRF
+7F-7Y -30G+30S ($allF^{30GtoS}$)	GSMASASSSQRSRSSSGNFSGSRSGSFSGNDNFGRSGNFSGRSGFSGSRSGSGFSGSSDSF NSFGNDSSNFSGSSSFNDFGNFNNQSSNFGPMKSGNFSGRSSSSSGSSGQFFAKPRNQGSF SGSSSSSSFSSSRRF
-23S+23T	GSMATATTTQRGRTGTGNFGGGRGGGFGGNDNFGRGGNFTGRGGFGGTRGGGGYGGTGDGY NGFGNDGTNFGGGGTYNDFGNYNNQTTNFGPMKGGNFGGRTTGGTGGGGQYFAKPRNQGGY GGTTTTTTYGTGRRF
-14N+14Q	GSMASASSSQRGRSGSGQFGGGRGGGFGGQDQFGRGGQFSGRGGFGGSRGGGGYGGSGDGY QGFGQDGSQFGGGGSYQDFGQYQQQSSQFGPMKGGQFGGRSSGGSGGGGQYFAKPRQQGGY GGSSSSSSYGSGRRF
-14N-4Q+18G	GSMASASSSGRGRSGSGGFGGGRGGGFGGGDGFGRGGGFSGRGGFGGSRGGGGYGGSGDGY GGFGGDGSGFGGGGSYGDFGGYGGGSSGFGPMKGGGFGGRSSGGSGGGGGYFAKPRGGGGY GGSSSSSSYGSGRRF
+7R+10D	GSMASADSSQRDRDGRGNFGDGRGGGFGGNDNFGRGGNFSDRGGFGGSRGGGRYGGDGDRY NGFGNDGRNFGGGGSYNDFGNYNNQSSNFDPMKGGNFRDRSSGPYDRGGQYFAKPRNQGGY GGSSSSRSYGSDRRF
+7R+12D	GSMASADSSQRDRDDRGNFGDGRGGGFGGNDNFGRGGNFSDRGGFGGSRGDGRYGGDGDRY NGFGNDGRNFGGGGSYNDFGNYNNQSSNFDPMKGGNFRDRSSGPYDRGGQYFAKPRNQGGY GGSSSSRSYGSDRRF
-10F +7R+12D	GSMASADSSQRDRDDRGNFGDGRGGGGGGNDNFGRGGNGSDRGGGGGSRGDGRYGGDGDRY NGGGNDGRNGGGGGSYNDGGNYNNQSSNGDPMKGGNGRDRSSGPYDRGGQYGAKPRNQGGY GGSSSSRSYGSDRRG
-12F+12Y-10R	GSMASASSSQGGSSGSGNYGGGGGGGYGGNDNYGGGGNYSGSGGYGGSGGGGGYGGSGDGY NGYGNDGSNYGGGGSYNDYGNYNNQSSNYGPMKGGNYGGSSSGPYGGGGQYYAKPGNQGGY GGSSSSSSYGSGGGY
-SYNDFG	GSMASASSSQRGRSGSGNFGGGRGGGFGGNDNFGRGGNFSGRGGFGGSRGGGGYGGSGDGY NGFGNDGSNFGGGGNYNNQSSNFGPMKGGNFGGRSSGGSGGGGQYFAKPRNQGGYGGSSSS SSYGSGRRF
FUS-LCD	GSMASNDYTQQATQSYGAYPTQPGQGYSQQSSQPYGQQSYSGYSQSTDTSGYGQSSYSSYG QSQNTGYGTQSTPQGYGSTGGYGSSQSSQSSYGQQSSYPGYGQQPAPSSTSGSYGSSSQSS SYGQPQSGSYSQQPSYGGQQQSYGQQQSYNPPQGYGQQNQYNSSSGGGGGGGGGNYGQDQ SSMSSGGGSGGGYGNQDQSGGGGSGGYGQQDRG

Supplementary References

1 Bremer, A. *et al.* Deciphering how naturally occurring sequence features impact the phase behaviours of disordered prion-like domains. *Nature Chemistry* **14**, 196-207, doi:10.1038/s41557-021-00840-w (2022).

2 Martin, E. W. *et al.* Valence and patterning of aromatic residues determine the phase behavior of prion-like domains. *Science* **367**, 694-699 (2020).

3 Milkovic, N. M. & Mittag, T. in *Intrinsically Disordered Proteins: Methods and Protocols* (eds Birthe B. Kragelund & Karen Skriver) 685-702 (Springer US, 2020).

4 Peran, I., Martin, E. W. & Mittag, T. Walking Along a Protein Phase Diagram to Determine Coexistence Points by Static Light Scattering. *Methods Mol Biol* **2141**, 715-730, doi:10.1007/978-1-0716-0524-0_37 (2020).

5 Alshareedah, I., Moosa, M. M., Pham, M., Potoyan, D. A. & Banerjee, P. R. Programmable viscoelasticity in protein-RNA condensates with disordered sticker-spacer polypeptides. *Nature communications* **12**, 1-14 (2021).

6 Savitzky, A. & Golay, M. J. E. Smoothing + Differentiation of Data by Simplified Least Squares Procedures. *Anal Chem* **36**, 1627-&, doi:DOI 10.1021/ac60214a047 (1964).

7 Bouchard, M., Zurdo, J., Nettleton, E. J., Dobson, C. M. & Robinson, C. V. Formation of insulin amyloid fibrils followed by FTIR simultaneously with CD and electron microscopy. *Protein Sci* **9**, 1960-1967, doi:10.1110/ps.9.10.1960 (2000).

8 Jimenez, J. L. *et al.* The protofilament structure of insulin amyloid fibrils. *Proc Natl Acad Sci U S A* **99**, 9196-9201, doi:10.1073/pnas.142459399 (2002).

9 Xu, J., Viasnoff, V. & Wirtz, D. Compliance of actin filament networks measured by particle-tracking microrheology and diffusing wave spectroscopy. *Rheologica Acta* **37**, 387-398, doi:10.1007/s003970050125 (1998).

10 Evans, R., Tassieri, M., Auhl, D. & Waigh, T. A. Direct conversion of rheological compliance measurements into storage and loss moduli. *Phys Rev E* **80**, 012501 (2009).

11 Mason, T. G., Ganesan, K., van Zanten, J. H., Wirtz, D. & Kuo, S. C. Particle Tracking Microrheology of Complex Fluids. *Phys Rev Lett* **79**, 3282-3285, doi:10.1103/PhysRevLett.79.3282 (1997).

12 Maier, T. & Haraszti, T. Python algorithms in particle tracking microrheology. *Chemistry Central Journal* **6**, 1-9 (2012).

13 Jawerth, L. *et al.* Protein condensates as aging Maxwell fluids. *Science* **370**, 1317-1323 (2020).

14 Thirumalai, D. & Mountain, R. D. Activated dynamics, loss of ergodicity, and transport in supercooled liquids. *Phys Rev E* **47**, 479-489, doi:10.1103/PhysRevE.47.479 (1993).

15 Derrida, B. Random-energy model: An exactly solvable model of disordered systems. *Physical Review B* **24**, 2613-2626, doi:10.1103/PhysRevB.24.2613 (1981).

16 Patel, A. *et al.* A liquid-to-solid phase transition of the ALS protein FUS accelerated by disease mutation. *Cell* **162**, 1066-1077 (2015).

17 Molliex, A. *et al.* Phase separation by low complexity domains promotes stress granule assembly and drives pathological fibrillization. *Cell* **163**, 123-133 (2015).

18 Mathieu, C., Pappu, R. V. & Taylor, J. P. Beyond aggregation: Pathological phase transitions in neurodegenerative disease. *Science* **370**, 56-60, doi:doi:10.1126/science.abb8032 (2020).

19 Yi, S. *et al.* Solid/liquid coexistence during aging of FUS condensates. *bioRxiv*, 2022.2008.2015.503964, doi:10.1101/2022.08.15.503964 (2022).

20 Lu, S. *et al.* Heat-shock chaperone HSPB1 regulates cytoplasmic TDP-43 phase separation and liquid-to-gel transition. *Nature Cell Biology* **24**, 1378-1393, doi:10.1038/s41556-022-00988-8 (2022).

21 Maltseva, D. *et al.* Fibril formation and ordering of disordered FUS LC driven by hydrophobic interactions. *Nat Chem* **15**, 1146-1154, doi:10.1038/s41557-023-01221-1 (2023).

22 Choi, J.-M., Holehouse, A. S. & Pappu, R. V. Physical principles underlying the complex biology of intracellular phase transitions. *Annual Review of Biophysics* **49**, 107-133 (2020).
23 Farag, M. *et al.* Condensates formed by prion-like low-complexity domains have small-world network structures and interfaces defined by expanded conformations. *Nature Communications* **13**, 7722 (2022).
24 Farag, M., Borcherds, W. M., Bremer, A., Mittag, T. & Pappu, R. V. Phase separation of protein mixtures is driven by the interplay of homotypic and heterotypic interactions. *Nature Communications* **14**, 5527, doi:10.1101/2023.03.15.532828 (2023).
25 Eichinger, B. E. Configuration Statistics of Gaussian Molecules. *Macromolecules* **13**, 1-11, doi:10.1021/ma60073a001 (1980).
26 Yang, Y. & Yu, T. Graph theory of viscoelasticities for polymers with starshaped, multiple-ring and cyclic multiple-ring molecules. *Die Makromolekulare Chemie* **186**, 609-631, doi:https://doi.org/10.1002/macp.1985.021860315 (1985).
27 Rouse, P. E. A Theory of the Linear Viscoelastic Properties of Dilute Solutions of Coiling Polymers. *The Journal of Chemical Physics* **21**, 1272-1280, doi:10.1063/1.1699180 (1953).
28 Zimm, B. H. Dynamics of Polymer Molecules in Dilute Solution: Viscoelasticity, Flow Birefringence and Dielectric Loss. *The Journal of Chemical Physics* **24**, 269-278, doi:10.1063/1.1742462 (1956).
29 Peticolas, W. L. Introduction to the Molecular Viscoelastic Theory of Polymers and Its Applications. *Rubber Chemistry and Technology* **36**, 1422-1458, doi:10.5254/1.3539650 (1963).
30 Newman, M. *Networks: An Introduction*. (Oxford University Press, 2010).
31 Galvanetto, N. *et al.* Extreme dynamics in a biomolecular condensate. *Nature* **619**, 876-883, doi:10.1038/s41586-023-06329-5 (2023).
32 Alshareedah, I., Moosa, M. M., Pham, M., Potoyan, D. A. & Banerjee, P. R. Programmable viscoelasticity in protein-RNA condensates with disordered sticker-spacer polypeptides. *Nat Commun* **12**, 6620, doi:10.1038/s41467-021-26733-7 (2021).
33 Ruff, K., M., Harmon, T. S. & Pappu, R. V. CAMELOT: A machine learning approach for coarse-grained simulations of aggregation of block-copolymeric protein sequences. *The Journal of Chemical Physics* **143**, 243123, doi:10.1063/1.4935066 (2015).
34 Zeng, X. *et al.* Design of intrinsically disordered proteins that undergo phase transitions with lower critical solution temperatures. *APL Materials* **9**, doi:10.1063/5.0037438 (2021).
35 Boeynaems, S. *et al.* Spontaneous driving forces give rise to protein-RNA condensates with coexisting phases and complex material properties. *Proc Natl Acad Sci U S A* **116**, 7889-7898, doi:doi:10.1073/pnas.1821038116 (2019).
36 Wadsworth, G. M. & Banerjee, P. R. Phase-separation behaviour of RNAs. *Nature Chemistry* **15**, 1660-1661, doi:10.1038/s41557-023-01359-y (2023).
37 Sundaravadivelu Devarajan, D. *et al.* Sequence-dependent material properties of biomolecular condensates and their relation to dilute phase conformations. *Nature Communications* **15**, 1912, doi:10.1038/s41467-024-46223-w (2024).
38 Dignon, G. L., Zheng, W., Best, R. B., Kim, Y. C. & Mittal, J. Relation between single-molecule properties and phase behavior of intrinsically disordered proteins. *Proc Natl Acad Sci U S A* **115**, 9929, doi:10.1073/pnas.1804177115 (2018).
39 Schlenoff, J. B. & Akkaoui, K. Dissecting dynamics near the glass transition using polyelectrolyte complexes. *Macromolecules* **54**, 3413-3422 (2021).
40 Alshareedah, I., Singh, A., Quinn, A. & Banerjee, P. R. Determinants of Viscoelasticity and Flow Activation Energy in Biomolecular Condensates. *bioRxiv*, https://doi.org/10.1101/2022.1112.1130.522262 (2022).
41 Messaâdi, A. *et al.* A New Equation Relating the Viscosity Arrhenius Temperature and the Activation Energy for Some Newtonian Classical Solvents. *Journal of Chemistry* **2015**, 163262, doi:10.1155/2015/163262 (2015).

42 Harmon, T. S., Holehouse, A. S., Rosen, M. K. & Pappu, R. V. Intrinsically disordered linkers determine the interplay between phase separation and gelation in multivalent proteins. *eLife* **6**, 30294, doi:10.7554/eLife.30294 (2017).
43 Pappu, R. V., Cohen, S. R., Dar, F., Farag, M. & Kar, M. Phase Transitions of Associative Biomacromolecules. *Chemical Reviews* **123**, 8945-8987, doi:10.1021/acs.chemrev.2c00814 (2023).
44 Greinert, N., Wood, T. & Bartlett, P. Measurement of effective temperatures in an aging colloidal glass. *Phys Rev Lett* **97**, 265702, doi:10.1103/PhysRevLett.97.265702 (2006).
45 Xiao, R., Sun, H. & Chen, W. An equivalence between generalized Maxwell model and fractional Zener model. *Mechanics of Materials* **100**, 148-153, doi:https://doi.org/10.1016/j.mechmat.2016.06.016 (2016).
46 Landau, L. The Theory of Phase Transitions. *Nature* **138**, 840-841, doi:10.1038/138840a0 (1936).
47 Zwanzig, R. Diffusion in a rough potential. *Proceedings of the National Academy of Sciences USA* **85**, 2029-2030, doi:doi:10.1073/pnas.85.7.2029 (1988).
48 Posey, A. E. *et al.* Mechanistic Inferences From Analysis of Measurements of Protein Phase Transitions in Live Cells. *Journal of Molecular Biology* **433**, 166848, doi:https://doi.org/10.1016/j.jmb.2021.166848 (2021).
49 Dai, Y. *et al.* Programmable synthetic biomolecular condensates for cellular control. *Nat Chem Biol* **19**, 518-528, doi:10.1038/s41589-022-01252-8 (2023).
50 Holehouse, A. S., Ginell, G. M., Griffith, D. & Böke, E. Clustering of Aromatic Residues in Prion-like Domains Can Tune the Formation, State, and Organization of Biomolecular Condensates. *Biochemistry* **60**, 3566-3581, doi:10.1021/acs.biochem.1c00465 (2021).
51 Wang, J. *et al.* A Molecular Grammar Governing the Driving Forces for Phase Separation of Prion-like RNA Binding Proteins. *Cell* **174**, 688-699.e616, doi:10.1016/j.cell.2018.06.006 (2018).
52 Li, W. *et al.* Biophysical properties of AKAP95 protein condensates regulate splicing and tumorigenesis. *Nature cell biology* **22**, 960-972 (2020).
53 Shi, B. *et al.* UTX condensation underlies its tumour-suppressive activity. *Nature* **597**, 726-731, doi:10.1038/s41586-021-03903-7 (2021).
54 Alberti, S. & Hyman, A. A. Biomolecular condensates at the nexus of cellular stress, protein aggregation disease and ageing. *Nature Reviews Molecular Cell Biology* **22**, 196-213, doi:10.1038/s41580-020-00326-6 (2021).
55 Boke, E. *et al.* Amyloid-like Self-Assembly of a Cellular Compartment. *Cell* **166**, 637-650, doi:10.1016/j.cell.2016.06.051 (2016).
56 Wang, M. *et al.* Stress-Induced Low Complexity RNA Activates Physiological Amyloidogenesis. *Cell Reports* **24**, 1713-1721.e1714, doi:10.1016/j.celrep.2018.07.040 (2018).
57 Feric, M. *et al.* Coexisting Liquid Phases Underlie Nucleolar Subcompartments. *Cell* **165**, 1686-1697, doi:10.1016/j.cell.2016.04.047 (2016).
58 Feric, M. *et al.* Mesoscale structure–function relationships in mitochondrial transcriptional condensates. *Proc Natl Acad Sci U S A* **119**, e2207303119, doi:doi:10.1073/pnas.2207303119 (2022).
59 Lin, A. Z. *et al.* Dynamical control enables the formation of demixed biomolecular condensates. *Nature Communications* **14**, 7678, doi:10.1038/s41467-023-43489-4 (2023).